Suppression of effective spin-orbit coupling by thermal fluctuations in spin-orbit coupled antiferromagnets

Jan Lotze [1] and Maria Daghofer [1,2]

[1]*Institut für Funktionelle Materie und Quantentechnologien, Universität Stuttgart, 70550 Stuttgart, Germany*
[2]*Center for Integrated Quantum Science and Technology, University of Stuttgart, Pfaffenwaldring 57, 70550 Stuttgart, Germany*

We apply the finite-temperature variational cluster approach to a strongly correlated and spin-orbit coupled model for four electrons (i.e., two holes) in the t_{2g} subshell. We focus on parameters suitable for antiferromagnetic Mott insulators, in particular, Ca_2RuO_4, and identify a crossover from the low-temperature regime, where spin-orbit coupling is essential, to the high-temperature regime where it leaves few signatures. The crossover is seen in one-particle spectra, where xz and yz spectra are almost one dimensional (as expected for weak spin-orbit coupling) at high temperature. At lower temperature, where spin-orbit coupling mixes all three orbitals, they become more two dimensional. However, stronger effects are seen in two-particle observables like the weight in states with definite on-site angular momentum. We thus identify the enigmatic intermediate-temperature "orbital-order phase transition," which has been reported in various x-ray diffraction and absorption experiments at $T \approx 260$ K, as the signature of the onset of spin-orbital correlations.

I. INTRODUCTION

Ruthenium oxides have for decades attracted considerable attention, first for their complex phase diagrams that bear some similarities to those high-T_N cuprate superconductors, with superconducting and Mott-insulating phases [1]. More recently, the interplay of spin-orbit coupling (SOC), electron itinerancy, electronic correlations, and lattice degrees of freedom, which are all present, has attracted attention. The exotic behavior emerging on this stage includes a potential spin liquid in α-$RuCl_3$ [2,3], enigmatic superconductivity in Sr_2RuO_4 [4], and a nonequilibrium Weyl semimetal in Ca_2RuO_4 [5].

This last compound, Ca_2RuO_4, had already been discussed as a Mott-insulating end member of the family of compounds including enigmatic superconductors. Its high-temperature metal-insulator transition has been well described by a combination of density-functional theory and dynamical mean-field theory [6]. The emerging picture is that of a lattice-supported Mott transition, where the c-axis bond length is shortened so that the xy orbital is lowered in energy and becomes nearly doubly occupied [7,8], while a Mott gap opens in the approximately half-filled xz and yz orbitals. SOC, which had alternatively been argued to drive the metal-insulator transition [9], was later shown to have only a weak impact on the gap [6]. More recently, *ab initio* calculations performed in the context of nonequilibrium studies have corroborated the intimate relation of the c-axis bond length, and thus the resulting crystal field (CF), to the metal-insulator transition [10].

However, SOC turns out to be highly relevant for the magnetic properties of the antiferromagnetic state observed at even lower temperatures. For weak SOC and the dominant CF, one would expect the half-filled xz and yz orbitals to form a spin one, while the doubly occupied xy orbital would be magnetically inert. However, magnetic excitations turn out to show pronounced X-Y symmetry [12] as well as Higgs modes [13,16], which can more naturally be explained in terms of "excitonic" antiferromagnetism, which fundamentally relies on SOC. A basic sketch of the observed transitions is shown in Fig. 1.

The orbital angular momentum of two t_{2g} holes can be modeled as an effective $L = 1$. In the idealized picture of an undistorted Ru-O octahedron (i.e., with equivalent xy, yz, and xz orbitals), SOC would couple the total spin $S = 1$ with $L = 1$ into a singlet ground state with the total angular momentum $J = 0$ [17]. When superexchange connects ions, however, higher-energy triplets gain kinetic energy and may condense into a magnetically ordered state. In one dimension, the resulting ground-state phase diagram has been established by use of the density-matrix renormalization group and includes a parameter regime supporting excitonic magnetism [18,19]. Recent numerical work using a combination of density-functional theory and the variational cluster approach (VCA) has further indicated that the excitonic scenario with SOC as a decisive player indeed applies to the antiferromagnetic low-temperature state of Ca_2RuO_4 [20].

It would thus be highly desirable to investigate temperatures between the ground state with a large role for SOC and the high-temperature state, where it only yields small corrections, also with a view towards other ruthenates with similar energy scales. While the metal-insulator transition and the interplay of lattice and correlations is accessible to dynamical mean-field theory with a Monte-Carlo impurity solver, the fermionic minus-sign problem is present at lower temperatures [10]. Adjusted one-particle states based on the total angular momentum can reduce the minus-sign problem [21],
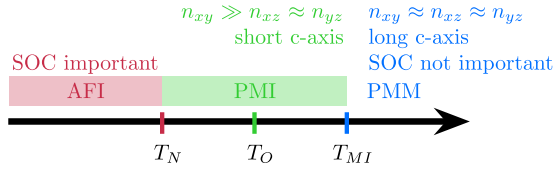
FIG. 1. Sketch of the temperature-driven phase transitions observed in Ca_2RuO_4. Below the Néel temperature $T_N \approx 110$ K [11], there is an antiferromagnetic insulator (AFI) with spins mostly lying in plane and with strong signatures of SOC in magnetic excitations [12,13]. The metal-insulator transition $T_{MI} \approx 360$ K separates insulating and metallic paramagnetic states (PMI and PMM). The metal-insulator transition also involves a shortening of the c-axis bond length and concomitant increase in xy occupation. (Note that even the "short" c bonds are considerably longer than the a and b bonds, as Ca_2RuO_4 is a layered material [22]). Between these two phase transitions, within the PMI phase, there is an additional transition at $T_O \approx 260$ K that affects orbital degrees of freedom, but does not change the unit cell [14,15].

however, such an optimal basis cannot easily be identified in realistic models, where CFs or anisotropic hoppings compete with SOC.

In order to address low-temperature scales of spin-orbit coupled t_{2g} orbitals, described by the three-orbital Hubbard model of Sec. II, we thus implement a finite-temperature variant of the VCA (see Sec. II A). Exact diagonalization is used to solve a small cluster and to extract its self energy, which is then used to evaluate the Green's function of the thermodynamic limit. This allows us to treat the antiferromagnetic order, and since we focus here on the Mott-insulating regime, bath sites are less necessary.

Based on the results presented in Sec. III, we identify a temperature range above the Néel temperature, but in the Mott-insulating regime, where the spin-orbital character strongly changes. While the on-site singlet and triplet states describe the ionic state at low temperatures very well, as expected for the excitonic scenario, they become less useful at higher temperatures. Here, the original orbitals provide a clearer picture, especially in the presence of a CF, as will be seen in the one-particle spectra discussed in Sec. III B.

In t_{2g} models with SOC of a magnitude suitable for excitonic magnetism, there is thus a third temperature scale intermediate between the metal-insulator transition related to charge fluctuations and lattice distortions and the Néel temperature related to magnetic degrees of freedom. We discuss in Sec. IV how this ties in with the enigmatic "orbital ordering" transition that has been debated at intermediate temperatures in Ca_2RuO_4 [14,15] (see also Fig. 1).

II. MODEL AND METHODS

We study here a three-orbital Hubbard model for t_{2g} electrons on a square lattice, where we focus on nearest-neighbor (NN) hopping and tetragonal symmetry. The kinetic energy is then diagonal in orbital indices and takes the form

$$H_{\text{kin}} = -t \sum_{\langle i,j \rangle,\sigma} c^\dagger_{i,xy,\sigma} c_{j,xy,\sigma} - t \sum_{\langle i,j \rangle \| x,\sigma} c^\dagger_{i,xz,\sigma} c_{j,xz,\sigma}$$
$$- t \sum_{\langle i,j \rangle \| y,\sigma} c^\dagger_{i,yz,\sigma} c_{j,yz,\sigma} + \text{H.c.}, \quad (1)$$

where $c_{i,\alpha,\sigma}$ ($c^\dagger_{i,\alpha,\sigma}$) annihilates (creates) an electron with spin $\sigma = \uparrow$ and $\downarrow$ in orbitals $\alpha = xy$, xz, and yz at site i. Nearest-neighbor bonds $\langle i, j \rangle$ along the two directions x and y are considered, as Ca_2RuO_4 is a layered compound [22], and we use $t \approx 0.2$ eV as our unit of energy.

Tetragonal CF splitting

$$H_{\text{CF}} = -\Delta \sum_{i,\sigma} n_{i,xy,\sigma} \quad (2)$$

with $n_{i,xy,\sigma} = c^\dagger_{i,xy,\sigma} c_{i,xy,\sigma}$ and $\Delta > 0$ is motivated by the shortened octahedra of the low-temperature phase of Ca_2RuO_4. For a filling of four electrons (two holes), it favors a doubly occupied xy orbital with half filled xz and yz orbitals. We tune it to interpolate between an orbitally polarized spin-one system at large Δ and a more equal interplay of degenerate orbitals at small Δ.

In the present paper, the impact of SOC is particularly important, which takes the form

$$H_{\text{SOC}} = \lambda \sum_i \mathbf{l}_i \cdot \mathbf{s}_i = \frac{i\lambda}{2} \sum_i \sum_{\substack{\alpha,\beta,\gamma \\ \sigma,\sigma'}} \varepsilon_{\alpha\beta\gamma} \tau^\alpha_{\sigma\sigma'} c^\dagger_{i,\beta,\sigma} c_{i,\gamma,\sigma'} \quad (3)$$

for t_{2g} orbitals, with the totally antisymmetric Levi-Civita tensor $\varepsilon_{\alpha\beta\gamma}$ and Pauli matrices τ^α, $\alpha = x$, y, and z [23,24]. We focus here on intermediate SOC that is not strong enough to suppress magnetic ordering.

Finally, there are effective on-site Coulomb interactions [25]:

$$H_{\text{int}} = U \sum_{i,\alpha} n_{i\alpha\uparrow} n_{i\alpha\downarrow} + \frac{U'}{2} \sum_{i,\sigma} \sum_{\alpha \neq \beta} n_{i\alpha\sigma} n_{i\beta\bar\sigma}$$
$$+ \frac{1}{2}(U' - J_H) \sum_{i,\sigma} \sum_{\alpha \neq \beta} n_{i\alpha\sigma} n_{i\beta\sigma}$$
$$- J_H \sum_{i,\alpha \neq \beta} (c^\dagger_{i\alpha\uparrow} c_{i\alpha\downarrow} c^\dagger_{i,\beta\downarrow} c_{i\beta\uparrow} - c^\dagger_{i\alpha\uparrow} c^\dagger_{i\alpha\downarrow} c_{i\beta\downarrow} c_{i\beta\uparrow}), \quad (4)$$

with Coulomb interactions U and U' and Hund's coupling J_H connected via $U' = U - 2J_H$. We are here less interested in varying interactions and rather focus on the Mott-insulating regime with a Hund's-rule coupling larger than SOC, so that **L**-**S** coupling provides a clearer description than j-j coupling. We thus choose $U = 12.5t$ and $J_H = 2.5t$, which is consistent with their order of magnitude in Ca_2RuO_4 [26].

A. Finite-temperature variational cluster approach

We use the finite-temperature [27] VCA [28,29], where the grand potential Ω of the system is approximated in terms of a "reference system" that consists of small disconnected clusters, but has the same electron-electron interactions as the Hamiltonian of interest [30]:

$$\Omega(\Sigma_{\text{cl}}) = \Omega_{\text{cl}} + \text{Tr} \ln \left(-G^{-1}_{\text{cl}} \right) - \text{Tr} \ln \left(-G^{-1}_{\text{CPT}} \right), \quad (5)$$

with the grand potential Ω_{cl} and Green's function G_{cl} obtained from the cluster. The cluster-perturbation-theory (CPT) Green's function $G^{-1}_{\text{CPT}} = (G^{-1}_{\text{cl}} - G^{-1}_{\text{cl},0} + G^{-1}_0)^{-1}$ replaces the noninteracting cluster Green's function $G_{\text{cl},0}$ by the noninteracting Green's function G_0 of the full system. The

approximation thus consists of replacing the self energy of the physical system by that of the small cluster. In order to improve the approximation, the self-energy–functional approach [29] allows us to optimize the cluster self energy Σ_{cl} by varying one-particle parameters of the reference Hamiltonian. The best approximation to the system's grand potential is a stationary point of Ω with respect to the variational one-particle parameters. Note that this variation affects only the small cluster; the noninteracting Green's function given by the one-particle part of the physical Hamiltonian remains fixed.

We numerically evaluate the cluster grand potential

$$\Omega_{cl} = -\beta^{-1} \ln(\Xi) = -\beta^{-1} \ln \sum_m e^{-\beta \varepsilon_m} \qquad (6)$$

with partition function Ξ and cluster energies ε_n, as well as the cluster Green's function, whose electron part reads

$$[G_{cl}^{(+)}]_{\alpha\beta}(z) = \sum_{m,n} \frac{e^{-\beta \varepsilon_m}}{\Xi} \left[\frac{\langle \Psi_m | c_\alpha | \Psi_n^+ \rangle \langle \Psi_n^+ | c_\beta^\dagger | \Psi_m \rangle}{z - E_{nm}^+ + i0^+} \right] \qquad (7)$$

with the energy difference $E_{nm}^\pm = \varepsilon_n^\pm - \varepsilon_m$. We largely follow Seki *et al.* [27] and obtain the spectrum and eigenstates with band Lanczos to resolve (approximately) degenerate eigenenergies. We use eight starting vectors and converge 120 eigenvectors, which are used to evaluate the Green's functions in a second Lanczos run. In this second step, band Lanczos did not turn out to be advantageous, and we thus use the conventional algorithm.

Assembling the cluster Green's function is accelerated with the help of a high-frequency expansion for frequency arguments with absolute values larger than that of the largest pole [27]. [Other frequencies are obtained via Eq. (7).] Following Seki *et al.* [27], the high-energy Green's function is expanded to 15th order as

$$G_{\alpha\beta}(z) = \sum_{k=0}^{\infty} \frac{M_{\alpha\beta}^{(k)}}{z^{k+1}} \qquad (8)$$

with moments $M_{\alpha\beta}^{(0)}(z) = \delta_{\alpha\beta}$ and

$$M_{\alpha\beta}^{(k>0)} = \sum_{m,n} (E_{nm}^+)^k \frac{e^{-\beta \varepsilon_m}}{\Xi} \langle \Psi_m \, | \, c_\alpha \, | \, \Psi_n^+ \rangle \langle \Psi_n^+ \, | \, c_\beta^\dagger \, | \, \Psi_m \rangle$$
$$+ \sum_{m,n} (-E_{nm}^-)^k \frac{e^{-\beta \varepsilon_m}}{\Xi} \langle \Psi_m \, | \, c_\beta^\dagger \, | \, \Psi_n^- \rangle \langle \Psi_n^- \, | \, c_\alpha \, | \, \Psi_m \rangle. \qquad (9)$$

In order to fix the density to $N = 4$ electrons (i.e., two holes), the grand potential is transformed to the free energy $F(N, V, T) = \Omega(\mu, V, T) + \mu N$ by means of a Legendre transform [31]. There are thus at least two variational parameters, the chemical potential μ to fix the density and the cluster chemical potential μ' to ensure thermodynamic consistency [32,33]. Additionally, we consider antiferromagnetic order parameters with ordered moment within the *a-b* plane or along the *c* axis. Previous work for $T = 0$ has shown that the *z* and in-plane components lead to quite different grand potentials (as expected for finite SOC), but that the grand potential is very similar for operators like spin, magnetization, or total angular momentum [20]. For this reason and in order

to easily compare to the spin-one antiferromagnet, we use here the spin as the order parameter. It has also been shown that a sizable CF as well as SOC both favor "checkerboard" magnetic patterns with ordering vector $\mathbf{Q} = (\pi, \pi)$, so that we use the fictitious Weiss field

$$H_{Weiss} = h \sum_i e^{i\mathbf{Q}\mathbf{r}_i} S_i^{x/z}, \qquad (10)$$

where *i* labels the site at $\mathbf{r}_i$ and $S_i^x = \sum_\alpha c_{i,\alpha,\uparrow}^\dagger c_{i,\alpha,\downarrow} + \text{H.c.}$ and $S_i^z = \sum_\alpha (c_{i,\alpha,\uparrow}^\dagger c_{i,\alpha,\uparrow} - c_{i,\alpha,\downarrow}^\dagger c_{i,\alpha,\downarrow})$ are the *x* and *z* components of the total spin, respectively.

For variational parameters μ, μ', and *h* giving stationary grand potentials, we evaluate one-body expectation values (like magnetization or orbital densities) from the Green's function, as is done for $T = 0$. The entropy *S* is determined as the derivative of the grand potential via contour integrals:

$$S = S_{cl} + \mathscr{S}_{CPT} + \mathscr{S}_{cl} - (\Omega_{CPT} - \Omega_{cl})/T, \qquad (11)$$

with the contributions

$$S_{cl} = -(\Omega_{cl} - \langle H \rangle_{cl})/T, \qquad (12)$$

$$\mathscr{S}_{CPT} = \oint_{\mathcal{C}} dz f(z) \text{tr}\big[\big(G_{cl} G_{CPT}^{-1} G_{cl} \big)^{-1} G_{mod} \big]/T^2, \qquad (13)$$

$$\mathscr{S}_{cl} = \oint_{\mathcal{C}} dz f(z) \text{tr}\big[\big(-G_{cl}^{-1} \big) G_{mod} \big]/T^2, \qquad (14)$$

and the abbreviations

$$\langle H \rangle_{cl} = \Xi^{-1} \sum_m \varepsilon_m \exp(-\beta \varepsilon_m), \qquad (15)$$

$$G_{mod} = \sum_{m,n} (\langle H \rangle_{cl} - \varepsilon_m) \Xi^{-1} \exp(-\beta \epsilon_m)[G_{cl}^+ + G_{cl}^-]$$
$$- \sum_{m,n} (Tz) \Xi^{-1} \exp(-\beta \epsilon_m) \left[\frac{\partial G_{cl}^+}{\partial z} + \frac{\partial G_{cl}^-}{\partial z} \right]. \qquad (16)$$

The specific heat $C(T)$ is then obtained as the numerical derivative $C(T) = \bar{T}(\Delta S / \Delta T)$ of the entropy.

Since the ordered moment in an excitonic magnet arises through a superposition of the $J = 0$ state preferred by on-site SOC and $J = 1$ states [17], it is helpful to consider the weights $\langle J \rangle$ found in eigenstates of the total on-site angular momentum *J*. Unfortunately, this is a two-particle quantity and thus not readily available from the VCA. We approximate it as the exact-diagonalization expectation value obtained for the N_{sites} sites of the reference cluster with optimized parameters:

$$\langle J \rangle := \frac{1}{N_{sites} \Xi} \sum_{i, J^z} \sum_m e^{-\beta \varepsilon_m} \langle m | J_i, J_i^z \rangle \langle J_i, J_i^z | m \rangle. \qquad (17)$$

Eigenstates $|J_i, J_i^z \rangle$ denote here the state at site *i* defined by the angular momentum $J = L + S$.

III. RESULTS

A. Temperature dependence of the on-site angular momentum

At $T = 0$, the VCA for the t_{2g} model with four electrons and the CF $\Delta = 0$ has revealed two different ordering patterns depending on λ [20]: at small $\lambda \lesssim 0.4\,t$, orbitals and spins order in a stripy pattern with orthogonal ordering momenta
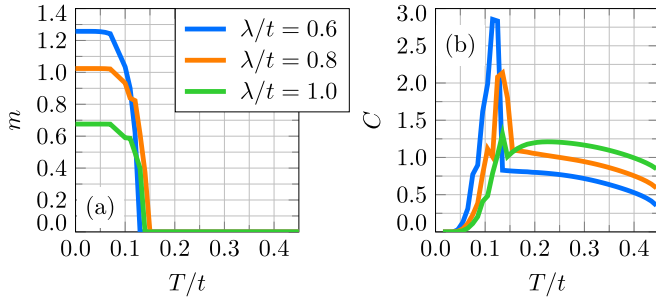
FIG. 2. Thermodynamics of the excitonic antiferromagnet without CF splitting. Panel (a) gives the magnetic order parameter, i.e., staggered out-of-plane spin and panel (b) gives the specific heat for SOC $\lambda = 0.6t$, $0.8t$, and t. (We do not intend to discuss the complicated spin and orbital stripe pattern found at $\lambda = \Delta = 0$ [20], and accordingly, we leave out the regime of small $\lambda \lesssim 0.4t$).

$(0, \pi)$ for spins and $(\pi, 0)$ for orbitals. For larger λ, the excitonic antiferromagnetic (AFM) order with momentum (π, π) takes over, where the out-of-plane z component is favored over in-plane directions. We are here interested in the latter regime and thus focus on $\lambda > 0.4t$.

Figure 2(a) shows the ordered spin moment depending on temperature. As expected, the value at $T = 0$ is reduced when larger λ increases the energy gap between the ionic singlet and triplet states, which in turn reduces the triplet admixture into the ground state. Somewhat surprisingly, the Néel temperature is not monotonic. While we can certainly not exclude strong finite-size effects due to the 2×1 site cluster, an alternative explanation may be that the system at the smallest $\lambda = 0.6t$ is affected by its closeness to the competing stripy phase. The corresponding specific heat is given in Fig. 2(b) and has a second broad hump at higher temperature $T > T_N$ in addition to the expected peak at the magnetic ordering transition. This feature exists for all three values of λ and shifts to slightly higher temperatures for $\lambda = t$.

Figure 3 shows the average weight Eq. (17) found in eigenstates with $J = 0$, 1, and 2 of the total on-site angular momentum. Weights are constant in the regime of constant magnetization, and the $J = 0$ ($J = 1$) state loses (gains) weight when the magnetic order is lost. This is in clear contrast to a (somewhat artificial) transition to a paramagnet at constant temperature: reducing the ordering field h at $T = 0$ pushes weight from the $J = 1$ states into the $J = 0$ state [20]. At T_N, the curves get abruptly steeper and weights in $J = 0$
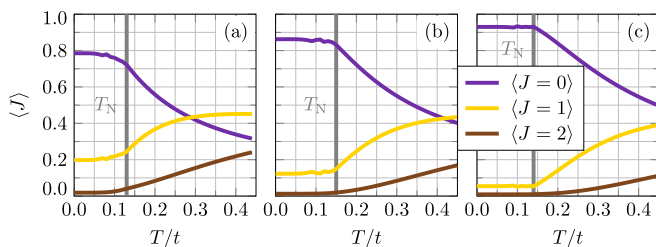

FIG. 3. Temperature evolution of the average weight found in eigenstates of the total angular momentum [see Eq. (17)]. (a) $\lambda = 0.6t$, (b) $\lambda = 0.8t$, and (c) $\lambda = t$.
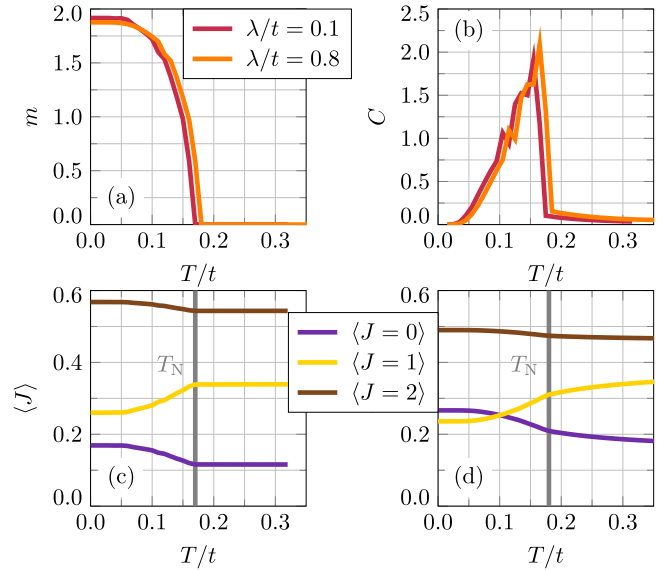

FIG. 4. Thermodynamics of the spin antiferromagnet at the large CF $\Delta = 5t$. Panel (a) gives the magnetic order parameter, i.e., staggered magnetization, and panel (b) gives the specific heat for SOC $\lambda = 0.1t$ and $\lambda = 0.8t$. ($\lambda = 0$ was numerically less stable). Panels (c) and (d) give the average overlaps of Eq. (17) for $\lambda = 0.1t$ and $\lambda = 0.8t$, respectively.

and $J = 1$ states change substantially at higher temperatures $T > T_N$. Weight in the $J = 2$ states is completely negligible below T_N, but similarly begins to grow at $T > T_N$. We are going to argue that this spin-orbital rearrangement is the origin of the second hump in the specific heat.

For comparison, Fig. 4(a) gives the magnetization and the specific heat for the CF $\Delta = 5t$ that is large enough to enforce complete orbital polarization with a doubly occupied xy orbital at all temperatures shown. The two holes are then found in xz and yz orbitals and form a conventional spin one, with an ordered moment close to 2 in the AFM state. The specific heat shown in Fig. 4(b) has here only the peak at the Néel temperature and no further features. The expected weights of eigenstates with total on-site angular momenta $J = 0$, 1, and 2 are given in Figs. 4(c) and 4(d) and present a quite different picture from the excitonic case discussed in Fig. 3: while the weights in $J = 0$ and $J = 1$ states change appreciably below T_N, only little variation is seen above T_N.

Finally, Figs. 5 and 7 discuss intermediate $\Delta = 1.5t$, an order of magnitude appropriate to describe Ca_2RuO_4. Ground-state VCA calculations have here shown in-plane magnetic moments to be favored over out-of-plane moments [20], in agreement with the AFM state of Ca_2RuO_4. Again, the Néel temperature is not very sensitive to SOC λ while the ordered moment is substantially reduced by it. The system without SOC has the largest ordered moment close to 2 [see Fig. 5(a)]. As is discussed below, its xy orbital is completely filled below the Néel temperature [see Fig. 7(a)], so that it comes close to a spin-one scenario. Larger $\lambda \geqslant 0.6t$ reduce the ordered moment, which indicates that orbital polarization is not strong enough to quench SOC. The specific heat shown in Fig. 5(b) looks qualitatively much more similar to the
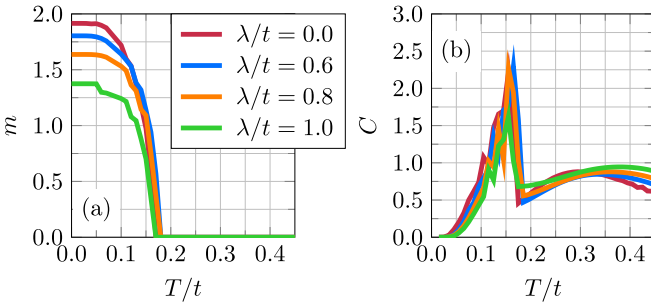
FIG. 5. Transition from spin to excitonic antiferromagnet at $\Delta = 1.5t$. Panel (a) gives the magnetic order parameter, i.e., staggered in-plane spin magnetization, and panel (b) gives the specific heat for SOC $\lambda = 0, 0.6t, 0.8t,$ and t.

FIG. 7. Spin-orbital on-site wave function for $\Delta = 1.5t$. Panels (a)–(d) show the orbital-resolved densities for $\lambda = 0, 0.6t, 0.8t,$ and t, and panels (e)–(h) show the weights in J states according to Eq. (17).

results for $\Delta = 0$ than to those for $\Delta = 5t$, as a second hump at $T > T_N$ is clearly seen.

The entropy is shown in Fig. 6, where no CF is compared with intermediate and large CFs at various values of SOC. For $T \to 0$, the entropy approaches 0 in all cases, as expected, and overall is similar in the magnetically ordered state for all scenarios. Above the Néel temperature T_N, the orbitally polarized system at large $\Delta = 5t$ is clearly different from absent or intermediate CFs. As can be seen in Fig. 6(c), the entropy above T_N is nearly constant for $\Delta = 5t$ and its value $S_1 = \log(\dim \mathcal{H})/(N_{\text{sites}} N_{\text{orbitals}}) = \log(495)/6$ is consistent with an effective spin-one system. For $\Delta = 0$ and $\Delta = 1.5t$ shown in Figs. 6(a) and 6(b), in contrast, the entropy continues to grow above T_N, indicating that more degrees of freedom become effectively available.

While the transition from spin-one to excitonic antiferromagnetism is a gradual crossover, it was estimated to occur at $\lambda \approx 0.7t$ in the ground state [20]. The J weights qualitatively agree, with Fig. 7(e) for $\lambda = 0$ being similar to the spin-one scenario of Figs. 4(c) and 4(d), while Figs. 7(g) and 7(h) for $\lambda = 0.8t$ and $\lambda = 1$ resemble more the excitonic case of Fig. 3. Figure 7(f) for $\lambda = 0.6t$ lies somewhere in between, again in line with the previous estimate.

The second hump in the specific heat for $\lambda = 0$ can be understood by noting that the orbital densities in Fig. 7(a) do not remain constant above T_N. Since the CF is now just strong enough to fill the xy orbital at $T = 0$, finite temperature can induce xy holes and these orbital fluctuations are reflected in the specific heat. The weights found in states $J = 0, 1,$ and 2, in contrast, do not change above T_N when there is no SOC [see Fig. 7(e)].

In the opposite limit $\lambda = t$, the orbital densities are nearly constant, a small difference between xz and yz below T_N being due to magnetic symmetry breaking. Weights in $J = 0$ and $J = 1$ states depend here strongly on temperature at $T > T_N$ [see Fig. 7(h)]. While low $T \lesssim T_N$ strongly suppressed any weight in $J = 2$ states for $\Delta = 0$ (see Fig. 3), it is here nearly constant, because it is connected to the clear orbital polarization $n_{xy} > n_{xz/yz}$ [20].

Finally, Fig. 8 corroborates that the specific-heat hump at higher temperatures arises from on-site effects. We have here based the VCA on the exact solution of a single site, so that correlations beyond on-site are explicitly excluded and do not include magnetic ordering. As a consequence, there are no magnetic intersite correlations that could induce triplet contributions and the ground state is given by the on-site singlet for $\Delta = 0$ [see Fig. 8(c)]. This is in agreement with earlier ground-state work [20] where magnetic solutions were also shown to have higher $J = 1$ content than nonmagnetic ones. (However, the earlier work addressed a cluster and thus still contained some intersite magnetic superexchange, so that some $J = 1$ character persisted). While the single-site cluster does thus not capture the magnetic low-temperature transition well, the higher-temperature features are in quite good agreement with the corresponding data obtained with the 2×1 site cluster.

B. Signatures of SOC in one-particle spectra

Figure 9 shows the VCA one-particle spectral density for $\Delta = 0$ and temperatures $T = 0$, $T \gtrsim T_N$, and $T \gg T_N$. At all temperatures, the occupied states are split into three sub-
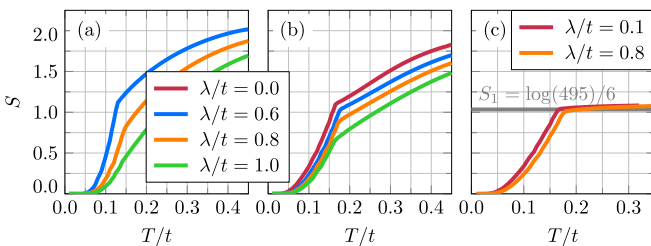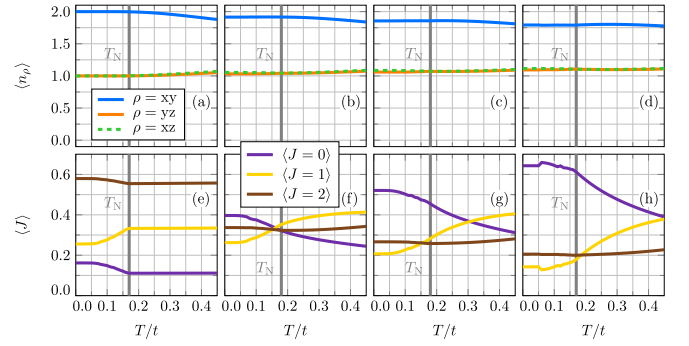

FIG. 6. Entropy depending on temperature for various values of λ and CFs (a) $\Delta = 0$, (b) $\Delta = 1.5t$, and (c) $\Delta = 5t$.
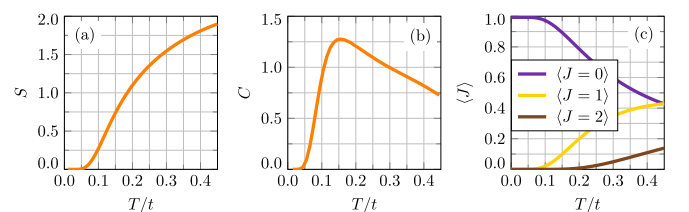

FIG. 8. (a) Entropy, (b) specific heat, and (c) weights in J states obtained with VCA based on the exact solution of a single site. $\Delta = 0$; $\lambda = 0.8t$.
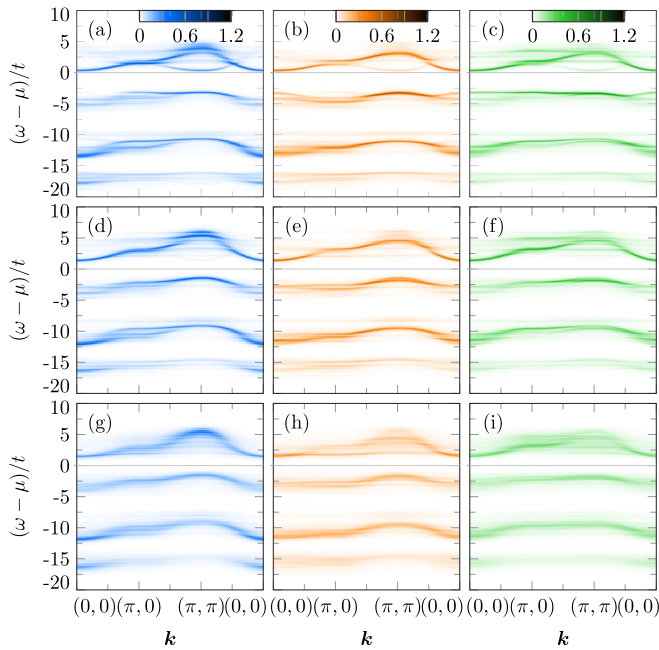
FIG. 9. Orbital-resolved one-particle spectral density for $\Delta = 0$, $\lambda = 0.8t$, and temperatures (a–c) $T = 0$, (d–f) $T = 0.14t \approx T_N$, and (g–i) $T = 0.35t$. The orbital character is xy in panels (a), (d), and (g); yz in panels (b), (e), and (h); and xz in panels (c), (f), and (i).

FIG. 10. Orbital-resolved one-particle spectral density for $\Delta = 1.5t$, $\lambda = t$, and temperatures (a–c) $T = 0$, (d–f) $T = 0.16t \approx T_N$, and (g–i) $T = 0.35t$. The orbital character is xy in panels (a), (d), and (g); yz in panels (b), (e), and (h); and xz in panels (c), (f), and (i).

bands at energies $\omega \lesssim 5t$, $\omega \approx 10t$, and $\omega \gtrsim 15t$ (with the last having lower weight), which can be related to Hund's-rule coupling [26]. Below T_N, some signatures of the doubling of the unit cell are visible in the form of shadow bands around $(0,0)$ and (π, π). Apart from this feature, the predominant effect of temperature is making the spectra less coherent. Overall, temperature effects on spectra are rather subtle.

Temperature-driven orbital reconstruction reveals itself slightly more when CF and SOC compete (see the one-particle spectra shown in Fig. 10 for $\Delta = 1.5t$ and $\lambda = t$). The ground-state spectrum in Figs. 10(a)–10(c) shows again a slight shadow band due to the doubling of the unit cell, and both the empty band (of predominantly xz and yz character) and the highest occupied band (of predominantly xy character) have a two-dimensional dispersion, similar to Figs. 9(a)–9(c). In the spectra taken around T_N [see Fig. 10(d)–10(f)], the shadow band has vanished. The occupied xz and yz states have become more coherent than in the ground state. This rather unconventional behavior may be related to the ladder-like features that were recently found in a strong-coupling t-J-like model without SOC, where they arise in the AFM state due to the anisotropic hoppings of these orbitals [34]: when magnetic order is lost, the ladder features become weaker and the underlying dispersion is seen more easily. It is rather one-dimensional, as expected for xz and yz orbitals without SOC. Such a weaker impact of SOC at higher binding energies is somewhat reminiscent of the correlation-induced energy dependence of SOC previously reported for metallic Sr_2RuO_4 [35].

In the *unoccupied* xz and yz states, on the other hand, incoherent features have gained weight in addition to the coherent band dominating the $T = 0$ spectrum. They do not follow the
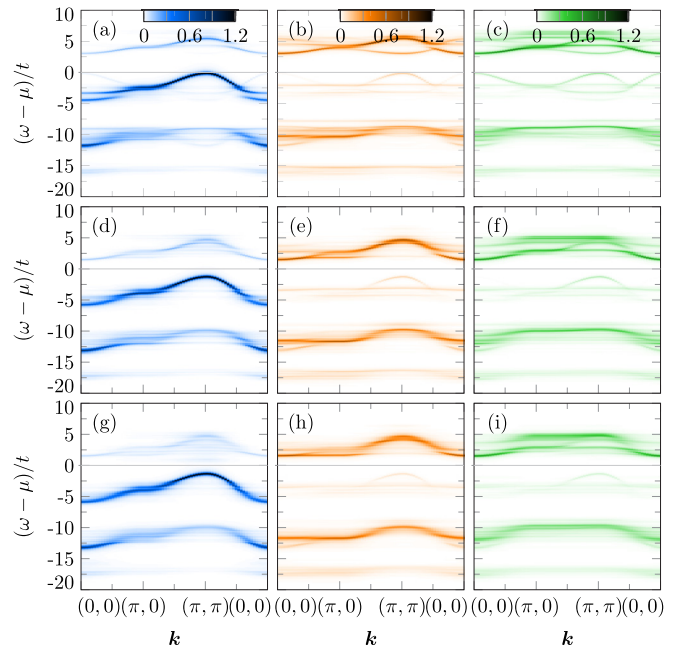
two-dimensional dispersion of the coherent band, but are more one dimensional. At high temperature $T = 0.35t$, finally, the unoccupied bands show mostly the one-dimensional dispersion characteristic of xz and yz orbitals in the absence of SOC [see Figs. 10(h)–10(i)]. In the presence of a CF, SOC thus only couples the three orbitals into a 2D dispersion at lower temperatures and lower excitation energies, while spectra at higher temperatures and energies look similar to the case without SOC.

IV. DISCUSSION AND CONCLUSIONS

We have shown that temperature strongly affects the spin-orbital on-site state in the PM Mott-insulating state of spin-orbit coupled t_{2g}^4 systems. We have investigated parameter sets supporting excitonic AFM order at low temperatures, with and without a crystal field. As long as the CF is not strong enough to completely quench the orbital degree of freedom, we consistently find a second broad hump in the specific heat, in addition to the peak at T_N. In the same temperature range, on-site total angular momentum changes substantially.

In one-particle spectra, low-energy excitations stemming from xz and yz orbitals are two-dimensional in the ground state, but become more one-dimensional at higher temperatures. This can also be interpreted as SOC being most effective at low temperatures. Overall, signatures of SOC and of the temperature-driven spin-orbital rearrangement are rather subtle in one-particle spectra. Even at low temperatures, where SOC is essential to reproduce the dispersion of magnetic excitations [13,16], one-particle spectra have thus been reasonably well described already without taking SOC into account [26,34].
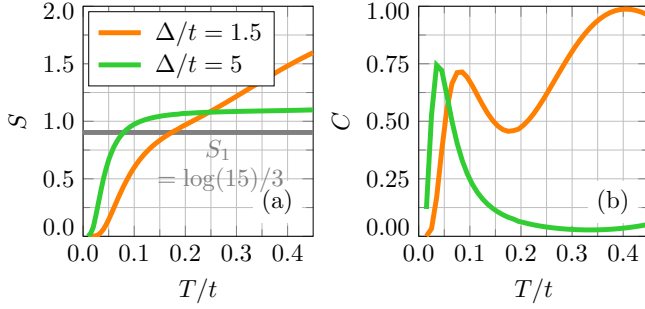
FIG. 11. (a) Entropy and (b) specific heat for SOC $\lambda = 0.8t$ at various CFs Δ.

However, we argue that x-ray diffraction and absorption experiments performed on Ca_2RuO_4 show signatures of the spin-orbital rearrangement found here. Parameters for this compound correspond roughly to those of Figs. 5(c), 5(d), and 10, i.e., $\Delta \approx 1.5t$ and $\lambda \approx 0.8t$–$1t$ [20]. At temperatures of ≈ 260 K, i.e., between the metal-insulator transition (which goes together with a structural phase transition) and the Néel transition, signatures of another phase transition were reported early on and interpreted in terms of orbital order [14,15].

Since this additional transition does not break any spatial symmetries, one can rule out orbital stripe [36] or checkerboard [37] patterns theoretically predicted for absent (or weak) SOC. More recent work established that the transition cannot be related to a change in orbital densities, leaving only the phase in a complex orbital superposition as a possibility [38]. This would fit with our findings of an SOC-driven spin-orbital rearrangement. When SOC prefers the $J = 0$ state at low temperatures, this implies for each spin projection a specific phase relation between the orbitals. In contrast, no
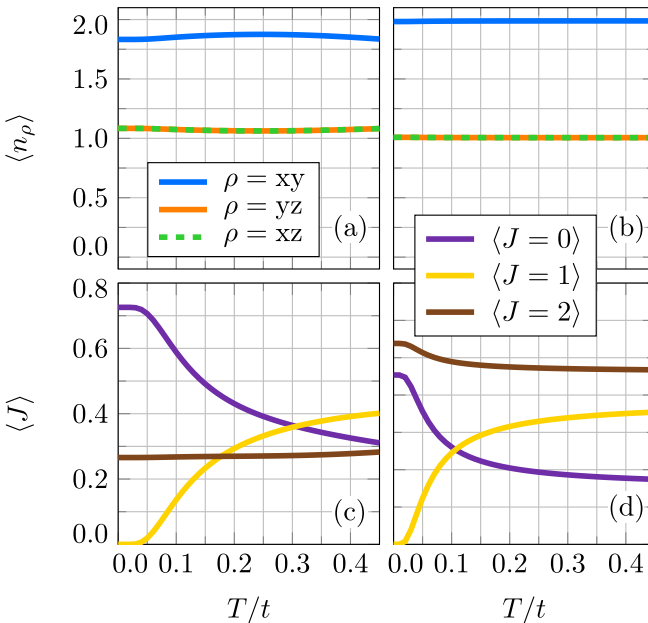
definite phases are expected at higher temperatures where SOC is less active.

We have thus identified the enigmatic orbital-order transition in Ca_2RuO_4 as a transition to a spin-orbit coupled on-site wave function. This implies, e.g., that a spin up (down) prefers the complex $|l^z = \pm 1\rangle$ orbital over the opposite state. This is somewhat reminiscent of a ferro-orbital order proposed early on for Ca_2RuO_4 [15], where the orbital wave function is a complex (rather than a real) superposition of t_{2g} orbitals. More generally, complex-orbital order has been suggested to play a role in doped manganites [39] and the Vervey transition of magnetite [40]. Spontaneous complex-orbital order is, however, rare, because lattice distortions like the Jahn-Teller effect favor real orbitals. The present work not only reconciles this picture with the observation of (nearly) constant density on xy orbitals in Ca_2RuO_4, but moreover shows the transition to arise naturally in a three-orbital model with SOC.

ACKNOWLEDGMENTS

APPENDIX: SINGLE-SITE VCA

To address the effect of different cluster sizes, we provide here additional observables for VCA based on a single site at moderate SOC $\lambda = 0.8t$ and different CFs. Due to the smaller system size, full diagonalization is employed and all eigenvectors are used for the trace. Since a single site cannot
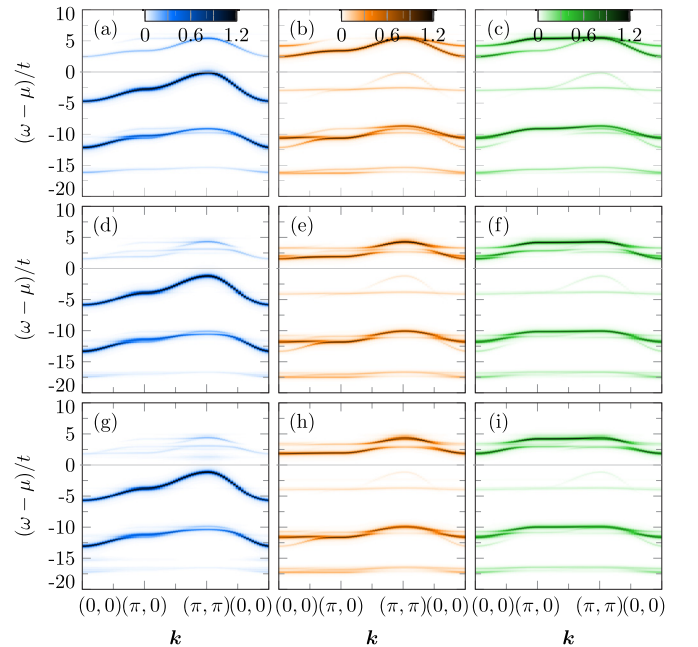

FIG. 12. Panels (a) and (b) show the orbital-resolved densities for $\Delta = 1.5t$ and $5t$, and panels (c) and (d) show the weights in J states according to Eq. (17). Both are at $\lambda = 0.8t$.

FIG. 13. Orbital-resolved one-particle spectral density for $\Delta = 1.5t$, $\lambda = 0.8t$, and temperatures (a–c) $T = 0$, (d–f) $T = 0.16t$, and (g–i) $T = 0.35t$. Orbital character is xy in panels (a), (d), and (g); yz in panels (b), (e), and (h); and xz in panels (c), (f), and (i).

support an AFM state, there is no ordering field and only physical and cluster chemical potentials are optimized.

Figure 11 shows the entropy and the specific heat. In agreement with the 2×1 site cluster, the entropy for $\Delta = 5t$ approaches a constant value consistent with an effective spin-one system. In the specific heat, a broad hump at elevated temperature exists only for moderate CF, but not for large CF. Compared to the 2×1 site cluster, the first peak in the specific heat is shifted to smaller temperature and less pronounced, presumably because AFM ordering is suppressed.

Similar to the results for the larger cluster shown in Fig. 7, orbital densities at intermediate CF $\Delta = 1.5t$ show pronounced orbital polarization that is only slightly, and non-monotonously, affected by increasing temperatures. Orbital polarization is complete for large CF [Fig. 12(b)] and absent

for $\Delta = 0$ (not shown), both in agreement with the larger cluster. Weights in total-angular-momentum states are shown in Figs. 12(c) and 12(d) and again qualitatively agree with results from the larger cluster, especially concerning the sequence of states and the temperatures where they cross. Increasing temperature increases the occupation of the $J = 1$ state mostly at the expense of the $J = 0$ state.

Figure 13 shows the spectral function based on a single site for intermediate CF $\Delta = 1.5t$. Compared to the results obtained from a 2×1 site cluster (see Fig. 10), the shadow bands are no longer present, because only the paramagnetic phase is considered. The transition from a two-dimensional dispersion at low temperature to a one-dimensional dispersion at higher temperature, however, remains. This can best be seen in the unoccupied states with dominant yz and xz weight.

[1] A. P. Mackenzie and Y. Maeno, The superconductivity of Sr_2RuO_4 and the physics of spin-triplet pairing, Rev. Mod. Phys. **75**, 657 (2003).

[2] K. W. Plumb, J. P. Clancy, L. J. Sandilands, V. V. Shankar, Y. F. Hu, K. S. Burch, H.-Y. Kee, and Y.-J. Kim, α-$RuCl_3$: A spin-orbit assisted Mott insulator on a honeycomb lattice, Phys. Rev. B **90**, 041112(R) (2014).

[3] Y. Kubota, H. Tanaka, T. Ono, Y. Narumi, and K. Kindo, Successive magnetic phase transitions in α-$RuCl_3$: xy-like frustrated magnet on the honeycomb lattice, Phys. Rev. B **91**, 094422 (2015).

[4] A. Pustogow, Y. Luo, A. Chronister, Y.-S. Su, D. A. Sokolov, F. Jerzembeck, A. P. Mackenzie, C. W. Hicks, N. Kikugawa, S. Raghu, E. D. Bauer, and S. E. Brown, Constraints on the superconducting order parameter in Sr_2RuO_4 from oxygen-17 nuclear magnetic resonance, Nature (London) **574**, 72 (2019).

[5] C. Sow, S. Yonezawa, S. Kitamura, T. Oka, K. Kuroki, F. Nakamura, and Y. Maeno, Current-induced strong diamagnetism in the Mott insulator Ca_2RuO_4, Science **358**, 1084 (2017).

[6] G. Zhang and E. Pavarini, Mott transition, spin-orbit effects, and magnetism in Ca_2RuO_4, Phys. Rev. B **95**, 075145 (2017).

[7] A. Liebsch and H. Ishida, Subband Filling and Mott Transition in $Ca_{2-x}Sr_xRuO_4$, Phys. Rev. Lett. **98**, 216403 (2007).

[8] F. Petocchi, V. Christiansson, and P. Werner, Fully *ab-initio* electronic structure of Ca_2RuO_4, arXiv:2106.03689.

[9] G.-Q. Liu, Spin-orbit coupling induced Mott transition in $Ca_{2-x}Sr_xRuO_4$ ($0 \leqslant x \leqslant 0.2$), Phys. Rev. B **84**, 235136 (2011).

[10] J. Bertinshaw, N. Gurung, P. Jorba, H. Liu, M. Schmid, D. T. Mantadakis, M. Daghofer, M. Krautloher, A. Jain, G. H. Ryu, O. Fabelo, P. Hansmann, G. Khaliullin, C. Pfleiderer, B. Keimer, and B. J. Kim, Unique Crystal Structure of Ca_2RuO_4 in the Current Stabilized Semimetallic State, Phys. Rev. Lett. **123**, 137204 (2019).

[11] M. Braden, G. André, S. Nakatsuji, and Y. Maeno, Crystal and magnetic structure of Ca_2RuO_4: Magnetoelastic coupling and the metal-insulator transition, Phys. Rev. B **58**, 847 (1998).

[12] S. Kunkemöller, D. Khomskii, P. Steffens, A. Piovano, A. A. Nugroho, and M. Braden, Highly Anisotropic Magnon Dispersion in Ca_2RuO_4: Evidence for Strong Spin Orbit Coupling, Phys. Rev. Lett. **115**, 247201 (2015).

[13] S.-M. Souliou, J. Chaloupka, G. Khaliullin, G. Ryu, A. Jain, B. J. Kim, M. Le Tacon, and B. Keimer, Raman Scattering from Higgs Mode Oscillations in the Two-Dimensional Antiferromagnet Ca_2RuO_4, Phys. Rev. Lett. **119**, 067201 (2017).

[14] I. Zegkinoglou, J. Strempfer, C. S. Nelson, J. P. Hill, J. Chakhalian, C. Bernhard, J. C. Lang, G. Srajer, H. Fukazawa, S. Nakatsuji, Y. Maeno, and B. Keimer, Orbital Ordering Transition in Ca_2RuO_4 Observed with Resonant X-Ray Diffraction, Phys. Rev. Lett. **95**, 136401 (2005).

[15] T. Mizokawa, L. H. Tjeng, G. A. Sawatzky, G. Ghiringhelli, O. Tjernberg, N. B. Brookes, H. Fukazawa, S. Nakatsuji, and Y. Maeno, Spin-Orbit Coupling in the Mott Insulator Ca_2RuO_4, Phys. Rev. Lett. **87**, 077202 (2001).

[16] A. Jain, M. Krautloher, J. Porras, G. Ryu, D. Chen, D. Abernathy, J. Park, A. Ivanov, J. Chaloupka, G. Khaliullin, B. Keimer, and B. Kim, Nat. Phys. **13**, 633 (2017).

[17] G. Khaliullin, Excitonic Magnetism in Van Vleck-type d^4 Mott Insulators, Phys. Rev. Lett. **111**, 197201 (2013).

[18] N. Kaushal, J. Herbrych, A. Nocera, G. Alvarez, A. Moreo, F. A. Reboredo, and E. Dagotto, Density matrix renormalization group study of a three-orbital Hubbard model with spin-orbit coupling in one dimension, Phys. Rev. B **96**, 155111 (2017).

[19] N. Kaushal, R. Soni, A. Nocera, G. Alvarez, and E. Dagotto, BCS-BEC crossover in a $(t_{2g})^4$ excitonic magnet, Phys. Rev. B **101**, 245147 (2020).

[20] T. Feldmaier, P. Strobel, M. Schmid, P. Hansmann, and M. Daghofer, Excitonic magnetism at the intersection of spin-orbit coupling and crystal-field splitting, Phys. Rev. Res. **2**, 033201 (2020).

[21] T. Sato, T. Shirakawa, and S. Yunoki, Spin-orbital entangled excitonic insulator with quadrupole order, Phys. Rev. B **99**, 075117 (2019).

[22] G. Cao, S. McCall, M. Shepard, J. E. Crow, and R. P. Guertin, Magnetic and transport properties of single-crystal **Ca_2RuO_4**: Relationship to superconducting **Sr_2RuO_4**, Phys. Rev. B **56**, R2916 (1997).

[23] M. Cuoco, F. Forte, and C. Noce, Probing spin-orbital-lattice correlations in $4d^4$ systems, Phys. Rev. B **73**, 094428 (2006).

[24] R. Triebl, G. J. Kraberger, J. Mravlje, and M. Aichhorn, Spin-orbit coupling and correlations in three-orbital systems, Phys. Rev. B **98**, 205128 (2018).

[25] A. M. Oleś, Antiferromagnetism and correlation of electrons in transition metals, Phys. Rev. B **28**, 327 (1983).

[26] D. Sutter, C. G. Fatuzzo, S. Moser, M. Kim, R. Fittipaldi, A. Vecchione, V. Granata, Y. Sassa, F. Cossalter, G. Gatti, M. Grioni, H. M. Rønnow, N. C. Plumb, C. E. Matt, M. Shi, M. Hoesch, T. K. Kim, T.-R. Chang, H.-T. Jeng, C. Jozwiak *et al.*, Hallmarks of Hunds coupling in the Mott insulator Ca_2RuO_4, Nat. Commun. **8**, 15176 (2017).

[27] K. Seki, T. Shirakawa, and S. Yunoki, Variational cluster approach to thermodynamic properties of interacting fermions at finite temperatures: A case study of the two-dimensional single-band Hubbard model at half filling, Phys. Rev. B **98**, 205114 (2018).

[28] M. Potthoff, M. Aichhorn, and C. Dahnken, Variational Cluster Approach to Correlated Electron Systems in Low Dimensions, Phys. Rev. Lett. **91**, 206402 (2003).

[29] M. Potthoff, Self-energy-functional approach: Analytical results and the Mott-Hubbard transition, Eur. Phys. J. B **36**, 335 (2003).

[30] M. Potthoff, Self-Energy-Functional Theory, in *Strongly Correlated Systems–Theoretical Methods* (Springer, Berlin, 2012).

[31] M. Balzer and M. Potthoff, Variational cluster approach to ferromagnetism in infinite dimensions and in one-dimensional chains, Phys. Rev. B **82**, 174441 (2010).

[32] M. Aichhorn and E. Arrigoni, Weak phase separation and the pseudogap in the electron-doped cuprates, Europhys. Lett. **72**, 117 (2005).

[33] D. Sénéchal, An introduction to quantum cluster methods, arXiv:0806.2690.

[34] A. Kłosiński, D. V. Efremov, J. van den Brink, and K. Wohlfeld, Photoemission spectrum of Ca_2RuO_4: Spin polaron physics in an $S = 1$ antiferromagnet with anisotropies, Phys. Rev. B **101**, 035115 (2020).

[35] M. Kim, J. Mravlje, M. Ferrero, O. Parcollet, and A. Georges, Spin-Orbit Coupling and Electronic Correlations in Sr_2RuO_4, Phys. Rev. Lett. **120**, 126401 (2018).

[36] M. Cuoco, F. Forte, and C. Noce, Interplay of Coulomb interactions and *c*-axis octahedra distortions in single-layer ruthenates, Phys. Rev. B **74**, 195124 (2006).

[37] T. Hotta and E. Dagotto, Prediction of Orbital Ordering in Single-Layered Ruthenates, Phys. Rev. Lett. **88**, 017201 (2001).

[38] D. G. Porter, V. Granata, F. Forte, S. Di Matteo, M. Cuoco, R. Fittipaldi, A. Vecchione, and A. Bombardi, Magnetic anisotropy and orbital ordering in Ca_2RuO_4, Phys. Rev. B **98**, 125142 (2018).

[39] J. van den Brink and D. Khomskii, Orbital ordering of complex orbitals in doped Mott insulators, Phys. Rev. B **63**, 140416(R) (2001).

[40] H. Uzu and A. Tanaka, Complex-orbital order in Fe_3O_4 and mechanism of the Verwey transition, J. Phys. Soc. Jpn. **77**, 074711 (2008).